CT Image-Guided Electrical Impedance Tomography for Medical Imaging

Ziang Li, Jie Zhang, Dong Liu, and Jiangfeng Du

***Abstract*— This study presents a computed tomography (CT) image-guided electrical impedance tomography (EIT) method for medical imaging. CT is a robust imaging modality for accurately reconstructing the density structure of the region being scanned. EIT can detect electrical impedance abnormalities to which CT scans may be insensitive, but the poor spatial resolution of EIT is a major concern for medical applications. A cross-gradient method has been introduced for oil and gas exploration to jointly invert multiple geophysical datasets associated with different medium properties in the same geological structure. In this study, we develop a CT image-guided EIT (CEIT) based on the cross-gradient method. We assume that both CT scanning and EIT imaging are conducted for the same medical target. A CT scan is first acquired to help solve the subsequent EIT imaging problem. During EIT imaging, we apply cross gradients between the CT image and the electrical conductivity distribution to iteratively constrain the conductivity inversion. The cross-gradient based method allows the mutual structures of different physical models to be referenced without directly affecting the polarity and amplitude of each model during the inversion. We apply the CEIT method to both numerical simulations and phantom experiments. The effectiveness of CEIT is demonstrated in comparison with conventional EIT. The comparison shows that the CEIT method can significantly improve the quality of conductivity images.**

***Index Terms*— Computed tomography, cross-gradient function, electrical impedance tomography, lung imaging.**

I. Introduction

IT IS essential to create visual representations of the interior of the human body for clinical analysis and medical intervention. Each of the various existing medical imaging technologies generally measures different types of data and presents images associated with different physiological properties of the structures, organs, and tissues of the human body. The need to combine morphologic and functional information has motivated the development of multimodality imaging in the field of diagnostic imaging [1]. This scenario is similar to geophysical imaging employed to delineate oil and gas reservoirs in the earth; however, the geological scale is much larger than the human body. Seismic waves are sensitive to the interfaces between rock formations, but only the electrical properties are significantly different across the interface between oil and water [2]. The oil and gas industry has transitioned from single-modality geophysical imaging to joint multi-physical imaging, in which multiple geophysical datasets are processed simultaneously with the application of mutual constraints [3]–[5].

The challenge with multiple datasets is similar in both medical and geophysical imaging: how can different imaging processes dealing with entirely different physical properties of the same target be incorporated to affect one another? In 2003, two geophysicists in the UK, Luis Alonso Gallardo and Maxwell Azuka Meju, developed a novel technology that allows multiple imaging processes accounting for different properties of the same target to influence one another simultaneously by imposing cross gradients between two different models [3], [4]. More than 570 technical papers by researchers worldwide have been published following their approach investigating ways to solve various joint geophysical imaging problems. In 2019, Gallardo and Meju received the Reginald Fessenden Award from the Society of Exploration Geophysicists (SEG) for their breakthrough invention and joined a list of elite awardees beginning with Beno Gutenberg, who discovered Earth's core in 1913. In this study, we extend the cross-gradient technology developed by Gallardo and Meju for the field of oil and gas exploration to medical imaging with the specific intent of developing CT-guided electrical impedance tomography.

The advent of CT has revolutionized diagnostic radiology [6], [7]. CT is a structural imaging technology with a high spatial resolution. EIT is a relatively new technique intended for noninvasively imaging the electrical conductivity distribution within a human body [8], [9]. Animal and clinical studies have revealed that many diseases, such as cardiac arrhythmias, osteoporosis, and leukemia [10]–[12], are associated with electrical conductivity abnormalities. To date, this imaging approach has shown satisfactory results in certain functional imaging studies and may offer a certain advantage in tumor analysis compared with CT. However, EIT is not yet

Manuscript received November 5, 2019; revised December 4, 2019; accepted December 5, 2019. Date of publication December 10, 2019; date of current version June 1, 2020. This work was supported in part by the National Natural Science Foundation of China under Grant 41674120 and Grant 61871356. *(Corresponding author: Jie Zhang.)*

Z. Li is with the School of Earth and Space Sciences, University of Science and Technology of China, Hefei 230026, China (e-mail: lza666@mail.ustc.edu.cn).

J. Zhang is with the School of Earth and Space Sciences, University of Science and Technology of China, Hefei 230026, China, and also with the School of Life Sciences, Division of Life Sciences and Medicine, University of Science and Technology of China, Hefei 230026, China (e-mail: jzhang25@ustc.edu.cn).

D. Liu and J. Du are with the Hefei National Laboratory for Physical Sciences, Microscale and Department of Modern Physics, University of Science and Technology of China, Hefei 230026, China, with the CAS Key Laboratory of Microscale Magnetic Resonance, University of Science and Technology of China, Hefei 230026, China, and also with the Synergetic Innovation Center of Quantum Information and Quantum Physics, University of Science and Technology of China, Hefei 230026, China (e-mail: dong.liu@outlook.com; djf@ustc.edu.cn).

Digital Object Identifier 10.1109/TMI.2019.2958670

fully suitable for anatomical imaging due to its poor spatial resolution [9], [13].

Solving the EIT problem involves numerical forward modeling and inversion. One accurate solution for the forward modeling problem is the complete electrode model (CEM) [14], which considers both the shunting effect and the contact impedance of electrodes. In addition, the point electrode model (PEM) [15] is applied in many practical applications when the size of the electrodes is very small compared to the total boundary area. Several numerical methods have been employed for solving the theoretical forward modeling problem including the finite element method (FEM) [15], the finite volume method (FVM) [16], the finite difference method (FDM) [17], and the boundary element method (BEM) [18]. These algorithms have been successfully applied to EIT forward simulations.

The inverse problem in EIT is highly nonlinear and nonunique. Inverse algorithms in medical imaging are divided into two categories, i.e., dynamic algorithms (impedance variation) and static algorithms (absolute impedance) [19]–[21]. A single-pass back-projection algorithm is initially applied to solve the inverse problem in EIT [22]. The single-pass sensitivity matrix method has also been used [23], [24]. However, the single-pass back-projection and sensitivity matrix methods can be effective only for small perturbations. To address large impedance variations, sensitivity methods or multiple-pass back-projection algorithms must be applied to minimize an objective function that includes data misfit and model regularization. A modified Newton–Raphson method [20] that finds a discrete conductivity distribution by minimizing the squared data misfit is one of the most common iterative methods for solving the inverse EIT problem. A significant advance has been made in the field of geophysics to solve the iterative inverse problem without explicitly using a sensitivity matrix, and the computation is extremely fast for three-dimensional imaging [25], [26].

If the inverse problem is ill-posed, regularization is usually needed to constrain the solution. Many regularization methods, such as Tikhonov [27], edge-preserving [28], [29], total variation [30], sparse multiscale [31], compactness [32], and shape-based regularization [33]–[36], can help solve ill-posed imaging problems. A regularization method helps constrain the solution by adding a penalty function to the objective function, achieving a stable solution while simultaneously assuring a global spatial resolution to a certain extent [37]. We include the Tikhonov regularization method in our study to ensure stability of the solution.

In this study, inspired by geophysical imaging problems [38]–[43], we use a CT image to constrain the EIT imaging problem and improve the resolution by applying a novel technology invented for geophysical imaging called cross-gradient regularization, which helps maintain the similarity between different physical properties while allowing a different magnitude for each property value in the common imaging area [3], [44]–[47]. We derive the cross-gradient function and its sensitivity matrix in a finite element model. The cross-gradient function is then incorporated as a constraint in a nonlinear least-squares inverse problem along with Tikhonov regularization. The CT image-guided EIT method is first tested in two simulations: a blocky model and a thorax geometry model. It is then applied to four phantom models. The imaging quality is assessed systematically for both simulations and phantom experiments.

II. Methods

A. Forward Modeling

The EIT imaging problem begins with forward modeling. The forward problem that aims to obtain the voltage response caused by the injection of current is solved by CEM in this study.

The potential $\varphi(x, y)$ in the domain Ω can be modeled by the generalized Laplace equation

$$\nabla \cdot (\sigma(x, y)\nabla\varphi(x, y)) = 0, \quad (x, y) \in \Omega, \tag{1}$$

where $\sigma(x, y)$ is the conductivity distribution function.

The boundary conditions are as follows

$$\varphi(x, y)+z_l\sigma(x, y)\frac{\partial\varphi(x, y)}{\partial n} = U_l, \quad (x, y)\in e_l, \ l=1, \ldots, L, \tag{2}$$

$$\sigma(x, y)\frac{\partial\varphi(x, y)}{\partial n} = 0, \quad (x, y) \in \partial\Omega\backslash\bigcup_{l=1}^{L} e_l, \tag{3}$$

where z_l is the contact impedance between the electrodes and the imaged body, n represents the unit vector of the outward normal direction on the boundary of the measurement area, U_l is the potential at the electrode e_l, $\partial\Omega$ denotes the boundary of the measurement area, and L is the number of electrodes.

In addition, for a prescribed current pattern I_l, $l = 1, ..., L$,

$$\int_{e_l} \sigma(x, y)\frac{\partial\varphi(x, y)}{\partial n}dS = I_l. \tag{4}$$

Kirchhoff's Law and the choice of ground must be imposed to ensure the existence and uniqueness of the result,

$$\sum_{l=1}^{L} I_l = 0, \quad \sum_{l=1}^{L} U_l = 0. \tag{5}$$

The FEM realization is based on an equivalent coercive weak formulation of the complete electrode model [48].

B. Recording Geometry

The recording geometry of EIT describes the strategy of applying a source excitation to the imaging target. According to the type of source excitation, the potential can be driven by a current or voltage corresponding to the induction or injection pattern, respectively.

A PXI-based EIT recording geometry (Kuopio Impedance Tomography 4 (KIT4)) [49] is applied in this study. The KIT4 recording geometry consists of 16 electrodes, 4 of which are sink electrodes {1, 5, 9, 13}. The injections are carried out pairwise between one sink electrode and the other 15 electrodes, leading to a total of 54 injections when reciprocal injections are removed.

C. Inversion Theory

To fit the measured voltages according to the calculated data, the objective function of the EIT inverse problem is defined as

$$F(\mathbf{m}_E) = \|\mathbf{d}_E - S(\mathbf{m}_E)\|^2 + \|\alpha \mathbf{L}\mathbf{m}_E\|^2, \tag{6}$$

where $\mathbf{d}_E$ represents the voltage vector measured by electrodes, $S(\mathbf{m}_E)$ represents the voltage vector obtained by forward calculation, $\mathbf{m}_E$ is the conductivity vector, α is the coefficient of regularization, and $\mathbf{L}$ is the Tikhonov regularization matrix. A modified Newton–Raphson method is applied to minimize the objective function (6).

With a CT image available, and assuming that both the CT and EIT measurements cover the same imaging area, we are able to further improve the imaging problem of equation (6) by applying cross-gradients between CT values and conductivities. The cross-gradient function is incorporated as an additional constraint in a nonlinear least-squares problem formulation.

The modified objective function for CEIT is

$$F(\mathbf{m}_E) = \|\mathbf{d}_E - S(\mathbf{m}_E)\|^2 + \|\alpha \mathbf{L}\mathbf{m}_E\|^2 + \|\beta t(\mathbf{m}_E, \mathbf{m}_C)\|^2, \tag{7}$$

where β represents the cross-gradient coefficient, and $t(\mathbf{m}_E, \mathbf{m}_C)$ is the cross-gradient vector between the conductivity $\mathbf{m}_E$ and the CT value $\mathbf{m}_C$.

The cross-gradient function is given by

$$t(\mathbf{m}_E, \mathbf{m}_C) = \nabla \mathbf{m}_E \times \nabla \mathbf{m}_C. \tag{8}$$

Equation (8) has no discontinuity or singularity limits other than those encountered when adopting model parameterizations. Equation (8) can be expressed as

$$t(x, y) = \left(\frac{\partial m_E(x, y)}{\partial y}\right)\left(\frac{\partial m_C(x, y)}{\partial x}\right) - \left(\frac{\partial m_E(x, y)}{\partial x}\right) \times \left(\frac{\partial m_C(x, y)}{\partial y}\right). \tag{9}$$

Equation (9) can be discretized by the finite difference method depicted in Fig. 2a, yielding the formula

$$t \cong \frac{4}{\Delta x \Delta y}(m_{Ec}(m_{Cb} - m_{Cr}) + m_{Er}(m_{Cc} - m_{Cb}) + m_{Eb}(m_{Cr} - m_{Cc})), \tag{10}$$

where the second subscripts c, b, and r on m_E or m_C denote the center, bottom and right cells, respectively, in the heterogeneous 2D grid depicted in Fig. 2a. The Δx and Δy denote the horizontal and vertical dimensions, respectively, of the cells (Fig. 2a) and serve to normalize the grid differences in equation (10).

We solve equation (9) by using the finite element method. Fig. 1a represents a triangular element Ω_0 with conductivity σ for a piece-wise constant model mesh in FEM. The finite element modeling with linear approximation is equivalent to a linear electrical network that connects nodes [15]. For example, referring to Fig. 1, a first-order triangular element as shown in Fig. 1a is equivalent to the circuit given in Fig. 1b. The resistors K_{12}, K_{23}, and K_{31} are replaced by the middle

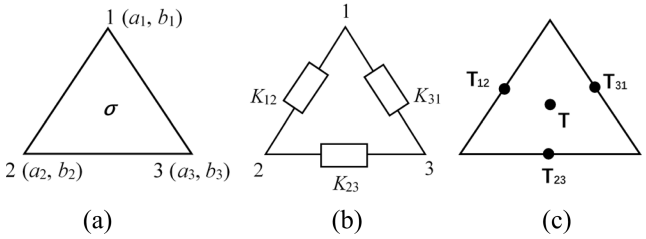

Fig. 1. Finite element model. (a) Triangular element and (b) its equivalent circuit. (c) Equivalent nodal model to (b).

nodes T_{12}, T_{23}, and T_{31} in Fig. 1c. The conductivity $\tilde{\sigma}$ on the element Ω_0 can be written as

$$\tilde{\sigma} = \lambda_1 + \lambda_2 x + \lambda_3 y, \tag{11}$$

where λ_1, λ_2, and λ_3 are the underdetermined coefficients.

Substituting the coordinates and conductivities of T_{12}, T_{23}, and T_{31} into equation (11), we have

$$\sigma = \lambda_1 + \lambda_2 \frac{a_1 + a_2}{2} + \lambda_3 \frac{b_1 + b_2}{2}, \tag{12}$$

$$\sigma = \lambda_1 + \lambda_2 \frac{a_3 + a_1}{2} + \lambda_3 \frac{b_3 + b_1}{2}, \tag{13}$$

$$\sigma = \lambda_1 + \lambda_2 \frac{a_2 + a_3}{2} + \lambda_3 \frac{b_2 + b_3}{2}. \tag{14}$$

We want to obtain the conductivity σ_T of the barycenter $T(\frac{a_1+a_2+a_3}{3}, \frac{b_1+b_2+b_3}{3})$. Adding equations (12)–(14), we have

$$\sigma = \lambda_1 + \lambda_2 \frac{a_1 + a_2 + a_3}{3} + \lambda_3 \frac{b_1 + b_2 + b_3}{3}. \tag{15}$$

Therefore, according to equations (11) and (15),

$$\sigma_T = \sigma. \tag{16}$$

We solve equation (9) based on the barycenter T depicted in Fig. 2b, and conductivity vector $\mathbf{m}_E$ is determined as

$$\mathbf{m}_E = \left(..., m_E^{k_0}, ...\right)^T, \quad k_0 \in \{1, \ldots, M\}, \tag{17}$$

where M is the number of elements in the finite element model.

According to Fig. 2b, we determine the gradient of $m_E^{k_0}$ as

$$\nabla m_E^{k_0} \cong \frac{m_E^{k_1} - m_E^{k_0}}{|\boldsymbol{l}_1|^2}\boldsymbol{l}_1 + \frac{m_E^{k_2} - m_E^{k_0}}{|\boldsymbol{l}_2|^2}\boldsymbol{l}_2 + \frac{m_E^{k_3} - m_E^{k_0}}{|\boldsymbol{l}_3|^2}\boldsymbol{l}_3, \tag{18}$$

where $m_E^{k_i}, i = 1, 2, 3, k_i \in \{1, \ldots, M\}$ represent conductivities of three adjacent elements, respectively. The $\boldsymbol{l}_1$, $\boldsymbol{l}_2$, and $\boldsymbol{l}_3$ are the vectors of the three separate directions, respectively.

$$\boldsymbol{l}_i = (x_i - x_0)\boldsymbol{i} + (y_i - y_0)\boldsymbol{j}, \quad i = 1, 2, 3, \tag{19}$$

where $\boldsymbol{i}$ and $\boldsymbol{j}$ are the unit vectors in the x and y directions, respectively.

In addition, the boundary conditions of the target area should be taken into account separately. We define the boundary problem for the cross-gradient function in Fig. 3. When we calculate the gradient for the boundary element of the two cases in Fig. 3, the gradient of the boundary element σ_1 can be calculated using the virtual element for which the conductivity is set to σ_1 (marked by the dashed line).

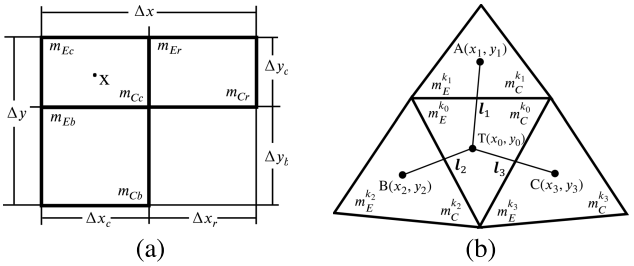

Fig. 2. (a) Definition of the $\mathbf{m}_E$–$\mathbf{m}_C$ cross-gradient function and its derivatives on a rectangular grid unit. For a 2D grid extending in the x and y directions, the function t is defined at the center of a given element (marked by a cross) taking into account the parameters from the two adjacent elements on its right (subscripted by 'r') and bottom (subscripted by 'b'). (b) Discretization of the $\mathbf{m}_E$–$\mathbf{m}_C$ cross-gradient function on a triangular grid unit. For a 2D grid extending in the $\boldsymbol{l}_1$, $\boldsymbol{l}_2$, and $\boldsymbol{l}_3$ directions, the function t is defined at the barycenter of a given element (marked by 'T') taking into account the parameters from the three adjacent elements (subscripted by 1–3). A, B, and C are the barycenters of the three elements.

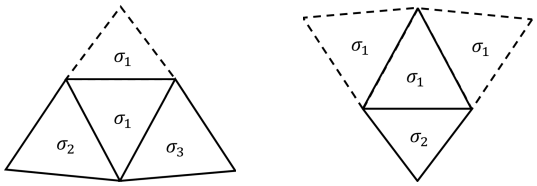

Fig. 3. Boundary definitions for the cross-gradient function.

Thus, we have

$$\nabla m_E^{k_0} = \left(\sum_{i=1}^{3} \frac{(m_E^{k_i} - m_E^{k_0})(x_i - x_0)}{(x_i - x_0)^2 + (y_i - y_0)^2}\right)\boldsymbol{i} + \left(\sum_{i=1}^{3} \frac{(m_E^{k_i} - m_E^{k_0})(y_i - y_0)}{(x_i - x_0)^2 + (y_i - y_0)^2}\right)\boldsymbol{j}, \tag{20}$$

$$\nabla m_C^{k_0} = \left(\sum_{i=1}^{3} \frac{(m_C^{k_i} - m_C^{k_0})(x_i - x_0)}{(x_i - x_0)^2 + (y_i - y_0)^2}\right)\boldsymbol{i} + \left(\sum_{i=1}^{3} \frac{(m_C^{k_i} - m_C^{k_0})(y_i - y_0)}{(x_i - x_0)^2 + (y_i - y_0)^2}\right)\boldsymbol{j}. \tag{21}$$

The gradients of $m_E^{k_0}$ and $m_C^{k_0}$ can also be written as

$$\nabla m_E^{k_0} = \frac{\partial m_E^{k_0}}{\partial x}\boldsymbol{i} + \frac{\partial m_E^{k_0}}{\partial y}\boldsymbol{j}, \tag{22}$$

$$\nabla m_C^{k_0} = \frac{\partial m_C^{k_0}}{\partial x}\boldsymbol{i} + \frac{\partial m_C^{k_0}}{\partial y}\boldsymbol{j}. \tag{23}$$

Comparing equations (20) and (22), we have

$$\frac{\partial m_E^{k_0}}{\partial x} = \sum_{i=1}^{3} \frac{(m_E^{k_i} - m_E^{k_0})(x_i - x_0)}{(x_i - x_0)^2 + (y_i - y_0)^2},$$
$$\frac{\partial m_E^{k_0}}{\partial y} = \sum_{i=1}^{3} \frac{(m_E^{k_i} - m_E^{k_0})(y_i - y_0)}{(x_i - x_0)^2 + (y_i - y_0)^2}. \tag{24}$$

Similarly, from equations (21) and (23), we have

$$\frac{\partial m_C^{k_0}}{\partial x} = \sum_{i=1}^{3} \frac{(m_C^{k_i} - m_C^{k_0})(x_i - x_0)}{(x_i - x_0)^2 + (y_i - y_0)^2},$$
$$\frac{\partial m_C^{k_0}}{\partial y} = \sum_{i=1}^{3} \frac{(m_C^{k_i} - m_C^{k_0})(y_i - y_0)}{(x_i - x_0)^2 + (y_i - y_0)^2}. \tag{25}$$

Substituting equations (24) and (25) into equation (9), we obtain the discrete representation of the cross-gradient function.

In the modified Newton–Raphson method, the sensitivity (Jacobian) matrix is calculated in the inversion process. According to equations (9), (24), and (25), the sensitivity matrix $\mathbf{A}$ of the cross-gradient function can be calculated directly by

$$\mathbf{A} = \begin{bmatrix} \cdots & \cdots & \cdots \\ \cdots & A_{k_0 k_0} & \cdots \\ \cdots & \cdots & \cdots \end{bmatrix}_{M \times M}, \tag{26}$$

where

$$A_{k_0 k_0} = \frac{\partial t}{\partial m_E^{k_0}} = \sum_{i=1}^{3} \frac{-(y_i - y_0)}{(x_i - x_0)^2 + (y_i - y_0)^2} \times \sum_{i=1}^{3} \frac{(m_C^{k_i} - m_C^{k_0})(x_i - x_0)}{(x_i - x_0)^2 + (y_i - y_0)^2} - \sum_{i=1}^{3} \frac{-(x_i - x_0)}{(x_i - x_0)^2 + (y_i - y_0)^2} \times \sum_{i=1}^{3} \frac{(m_C^{k_i} - m_C^{k_0})(y_i - y_0)}{(x_i - x_0)^2 + (y_i - y_0)^2}, \quad k_0 \in \{1, \ldots, M\}, \tag{27}$$

$$A_{k_0 k_j} = \frac{\partial t}{\partial m_E^{k_j}} = \frac{(y_j - y_0)}{(x_j - x_0)^2 + (y_j - y_0)^2} \times \sum_{i=1}^{3} \frac{(m_C^{k_i} - m_C^{k_0})(x_i - x_0)}{(x_i - x_0)^2 + (y_i - y_0)^2} - \frac{(x_j - x_0)}{(x_j - x_0)^2 + (y_j - y_0)^2} \times \sum_{i=1}^{3} \frac{(m_C^{k_i} - m_C^{k_0})(y_i - y_0)}{(x_i - x_0)^2 + (y_i - y_0)^2}, \quad j = 1, 2, 3, \; k_0, k_j \in \{1, \ldots, M\}, \tag{28}$$

$$A_{k_0 k} = \frac{\partial t}{\partial m_E^{k}} = 0, \quad k_0, k \in \{1, \ldots, M\}, \; k \notin \{k_0, k_1, k_2, k_3\}. \tag{29}$$

III. Simulations of a Blocky Model

We conduct numerical imaging of a simple blocky model that simulates the human thorax (Fig. 4). Three polygons are distributed within a circular boundary with a diameter of 2 cm. The background is homogenous. The analyses in this section involve noise-free data and address the issues of parameter selection, shape error, and insufficient information in the reference CT image. A starting model derived from the CT image for conventional EIT will be discussed as well.

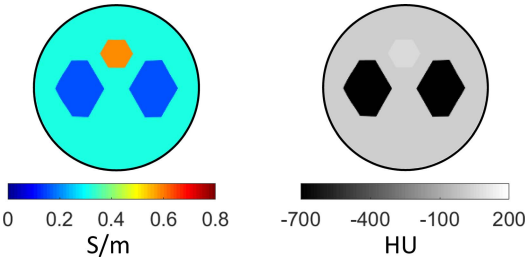

Fig. 4. A blocky distribution. True EIT model (left); the CT scan (right).

A. Modeling

In the numerical simulations, the measurement data are obtained by solving the forward problem described in Section II. The injected current is set to 1 A with a frequency of 10 kHz. Sixteen electrodes with a length of 0.22 cm are attached to the boundary of the target. The contact impedance is set to $1\times10^{-4}\ \Omega\cdot\mathrm{m}^2$ for all electrodes. The simulated conductivity and CT value distributions are shown in Fig. 4. The conductivities of the inclusions are set to 0.15 S/m for the two 'lung' objects, 0.6 S/m for the 'heart' object and 0.33 S/m for the background, corresponding to values found in the literature [50]. The CT values are set to −700 HU, 60 HU, and 30 HU for the 'lungs', 'heart', and background, respectively. A piecewise constant model with a mesh of 2,048 triangular elements and 1,089 nodes is employed for the forward calculations. The inversion applies a mesh of 1,023 elements and 620 nodes to avoid the so-called "inverse crime" [51]. All mesh models applied in this study are generated automatically according to [52]. A homogeneous conductivity model with $\sigma_0 = 0.33$ S/m is employed for both conventional EIT and CEIT as the starting model.

B. Quantitative Indicators

To quantitatively evaluate the reconstruction methods, the data (voltage) misfit and model (conductivity) misfit defined in equations (30) and (31) are calculated in this study. The data misfit is fundamental for evaluating the imaging results. When we apply imaging methods to physical experiments or clinical evaluations, the true distribution of the conductivity is usually unknown. A feasible approach for comparison is to use some shape indicators when the data misfit is at the same small level. The shape indicators widening (WD) and distortion (DT) were defined in previous EIT studies [53]. We revise the definitions of WD and DT in equations (32) and (33) so that the shape indicators are adequate for this study. WD is defined similarly to resolution. A WD value of 1 indicates an exact match of the areas between the true and recovered inclusions, while a value less than or greater than 1 would indicate underestimation or overestimation of the inclusion area. DT represents the shape deformation. A DT value of 0 indicates no shape deformations; the larger the DT, the more distorted the image.

Data Misfit:

$$\varepsilon_{data} = \sqrt{\frac{\sum_{i=1}^{N}(d_i^{Cal} - d_i^{Meas})^2}{N}}, \tag{30}$$

where d_i^{Cal} and d_i^{Meas} denote the calculated and measured voltage distributions, and N represents the total number of observations.

Model Misfit:

$$\varepsilon_{model} = \sqrt{\frac{\sum_{i=1}^{M}(m_i^{Cal} - m_i^{True})^2}{M}}, \tag{31}$$

where m_i^{Cal} and m_i^{True} are the inverted and true conductivity distributions, and M is the number of triangular elements.

WD:

$$\mathrm{WD} = \frac{\sum_{i=1}^{M} A_i^{Cal}}{\sum_{i=1}^{M} A_i^{True}}, \tag{32}$$

DT:

$$\mathrm{DT} = \frac{\sum_{i=1}^{M} \left|A_i^{Cal} - A_i^{True}\right|}{\sum_{i=1}^{M} A_i^{True}}, \tag{33}$$

where A_i^{Cal} is the shape parameter for the reconstructed targets, and A_i^{True} denotes the area of the true targets.

For the calculated conductivity distribution $\boldsymbol{\sigma}^{Cal}$ of the target area Γ,

if $\sigma_i^{Cal} > \sigma_0$, $i \in \Gamma$,

$$A_i^{Cal} = \begin{cases} 1, & for\ \sigma_i^{Cal} - \sigma_0 > 0.5\left(\max(\boldsymbol{\sigma}^{Cal}) - \sigma_0\right), \\ 0, & otherwise, \end{cases} \tag{34}$$

if $\sigma_i^{Cal} < \sigma_0$, $i \in \Gamma$,

$$A_i^{Cal} = \begin{cases} 1, & for\ \sigma_0 - \sigma_i^{Cal} > 0.5\left(\sigma_0 - \min(\boldsymbol{\sigma}^{Cal})\right), \\ 0, & otherwise. \end{cases} \tag{35}$$

In addition, for the true model $\boldsymbol{\sigma}^{True}$,

$$A_i^{True} = \begin{cases} 1, & for\ \sigma_i^{True} \neq \sigma_0, \\ 0, & otherwise, \end{cases} \tag{36}$$

where σ_0 denotes the assumed conductivity of the background.

C. Scaling Factors in CEIT

Appropriate scaling factors are important for obtaining accurate tomography results. For EIT, the regularization parameter α controls the trade-offs between the voltage error and the Tikhonov regularization term. On the other hand, the parameters α and β in CEIT control the trade-offs among the data misfit, the Tikhonov regularization term, and the cross-gradient function term. A series of scaling factors are tested in this study. Some of the results of the reconstruction are shown in Fig. 5. The corresponding choices of α and β are presented in Table I. The first row of Fig. 5 indicates the results

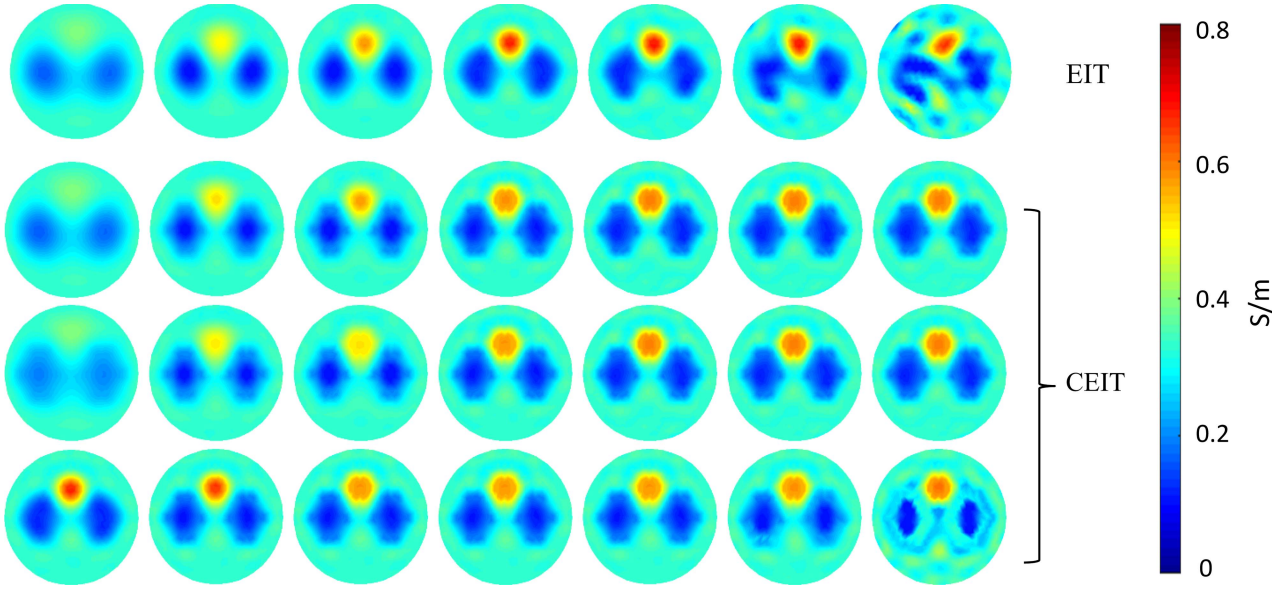

Fig. 5. Reconstructed images with different choices of α and β.

TABLE I
CHOICES OF α AND β

α	β	α	β	α	β	α	β	α	β	α	β	α	β
1	0	10^{-1}	0	10^{-2}	0	5×10^{-3}	0	3.236×10^{-3}	0	3.233×10^{-3}	0	3.231×10^{-3}	0
1	1	10^{-1}	1	10^{-2}	1	5×10^{-3}	1	3.236×10^{-3}	1	3.233×10^{-3}	1	3.231×10^{-3}	1
1	10	10^{-1}	10	10^{-2}	10	5×10^{-3}	10	3.236×10^{-3}	10	3.233×10^{-3}	10	3.231×10^{-3}	10
$\mathbf{5\times10^{-3}}$	10^{-2}	5×10^{-3}	10^{-1}	5×10^{-3}	10^{2}	5×10^{-3}	10^{4}	5×10^{-3}	10^{5}	5×10^{-3}	10^{6}	5×10^{-3}	2×10^{6}

of EIT when α equals 1, 0.1, 0.01, 0.005, 0.003236, 0.003233, and 0.003231, respectively. EIT can be used to reconstruct an overall image in any case with low resolution at the boundaries of the lung and heart. For larger α values, smoother images are obtained. The second and third rows are the results of CEIT when we fix β and choose different α. The boundaries of the objects are sharp and precise. In addition, when α is set to 0.003231, the result from EIT is distorted due to issues related to singular values. However, CEIT can provide a stable solution due to the cross-gradient constraints. The images in the fourth row show the results of a fixed α and varying β. If β is too small, the cross-gradient term cannot constrain the EIT image. If β is too large, the voltage data misfit cannot be reduced to a sufficiently small value, and the reconstructed model is inaccurate.

To select applicable scaling parameters α and β, the quantitative indicators for 90 different combinations of α and β are shown in Fig. 6. The red dashed line in the data misfit plot indicates the reliable area for the selection of α and β. Experience suggests $5 \times 10^{-3} < \alpha < 10^{-2}$ for achieving a good imaging quality for EIT. For CEIT, we determine the suitable parameters that $10^{-3} < \alpha < 5 \times 10^{-3}$ and $1 < \beta < 10^5$. In addition, the quantitative indicators show little difference when β varies from 1 to 10^5, which indicates the stability of the CEIT method to a wide range of values for the cross-gradient factor. We choose α equals 5×10^{-3} for EIT and α equals 10^{-3} and β equals 1 for CEIT to plot

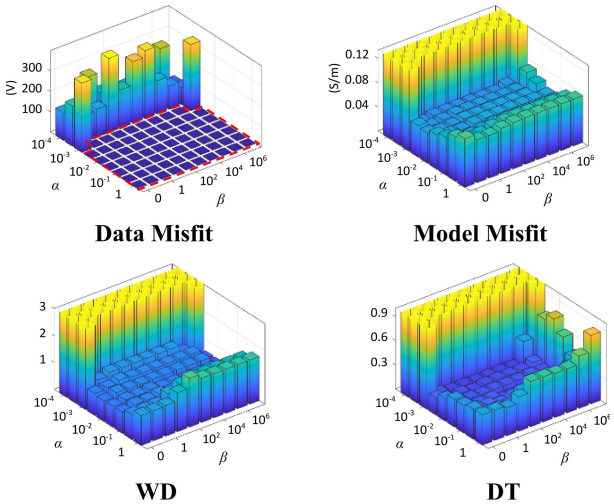

Fig. 6. Evolution of the quantitative indicators as functions of α and β.

the horizontal and vertical conductivity profiles in Fig. 7. The conductivity profiles obtained with EIT are smooth across the interfaces. The horizontal and vertical profiles show that CEIT improves the conductivity accuracy and enables reconstruction of large conductivity contrasts.

D. Shape Errors in Referenced CT Models

In practical applications of CEIT method, the synchronous acquisition of CT and electrical measurement data may be

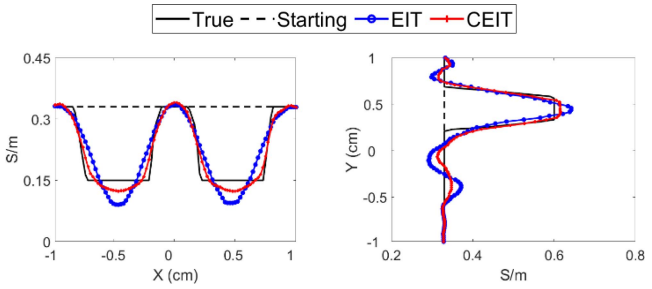

Fig. 7. Conductivity profiles. The horizontal conductivity profile of the model at y = 0 (left) and the vertical conductivity profile of the model at x = 0 (right).

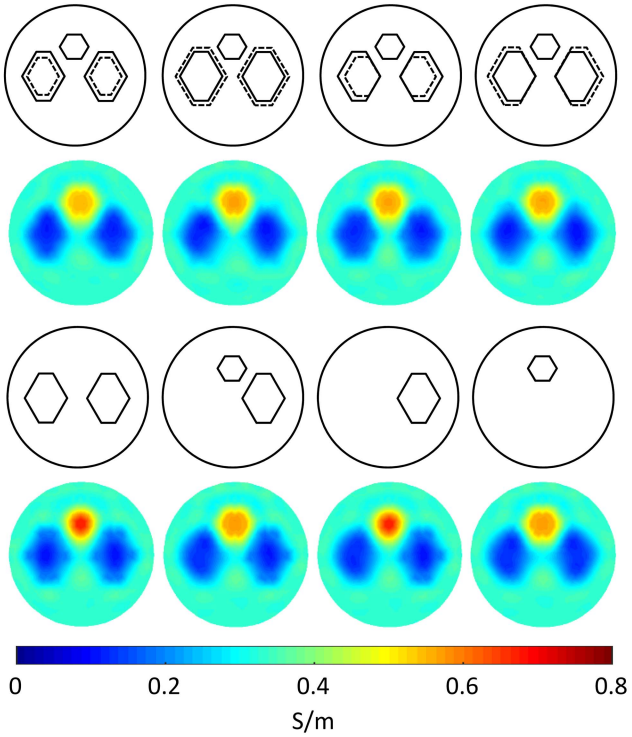

Fig. 8. Image reconstructions (Cases 1–8) with CT scans obtained from human respiration or movement (top), and incomplete structure descriptions (bottom).

challenging since human respiration or movement may cause inconsistent structural information between CT images and conductivity distributions. It is also difficult for the CT image to represent the entirety of the interior structures in the human body. For example, the CT value of a human heart is usually close to the soft tissue, and pleural effusion can also result in similar CT values between the lungs and soft tissue. We set α and β to 10^{-3} and 1, respectively, for CEIT. Four reconstruction images, corresponding to Cases 1–4, obtained by CEIT along with the model errors in the CT-scans caused by human respiration or movement are shown in the first and second rows, respectively, of Fig. 8. The third and fourth rows denote the results from Cases 5–8 by CEIT along with the model errors resulting from incomplete structure descriptions. The dashed lines in the plots denote the boundary changes from a 'perfect' CT scan to one with model errors. The quantitative

TABLE II
QUANTITATIVE INDICATORS OF THE RECOVERED INCLUSIONS

	Data Misfit (V)	Model Misfit (m/S)	WD	DT
Perfect CT scan	1.2×10^{-4}	4.3×10^{-2}	1.022	0.125
Case 1	1.0×10^{-4}	4.3×10^{-2}	1.113	0.193
Case 2	1.3×10^{-4}	4.3×10^{-2}	0.941	0.230
Case 3	1.1×10^{-4}	4.6×10^{-2}	1.086	0.152
Case 4	3.5×10^{-4}	4.6×10^{-2}	0.832	0.274
Case 5	9.0×10^{-5}	4.1×10^{-2}	1.012	0.135
Case 6	1.1×10^{-4}	4.3×10^{-2}	0.977	0.157
Case 7	8.3×10^{-5}	4.1×10^{-2}	0.955	0.174
Case 8	1.0×10^{-4}	4.3×10^{-2}	0.912	0.194

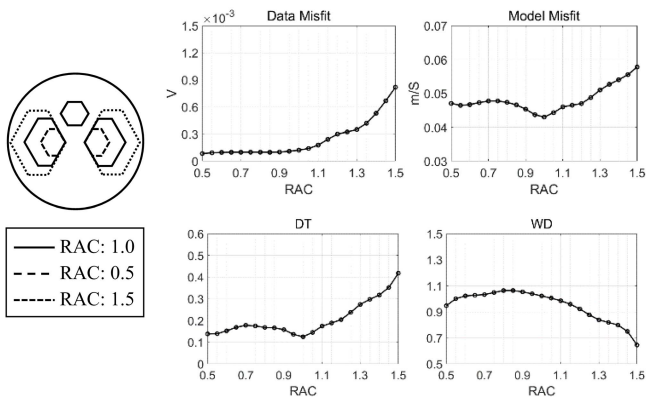

Fig. 9. Evolution of quantitative indicators (right) as a function of shape error (left).

indicators are shown in Table II. DT shows small fluctuations but WD is relatively stable to the model errors caused by the human respiration or movement. On the other hand, both WD and DT show acceptable variations to the model errors caused by the incomplete structure descriptions.

In addition, the shape errors caused by human respiration are quantitatively evaluated by the relative area change (RAC),

$$\text{RAC}=\frac{\text{Area of the CT scan with model errors}}{\text{Area of the perfect CT scan}}. \quad (37)$$

As shown in the first column of Fig. 9, the RAC value of the 'perfect' CT scan is assumed to be 1.0, and the end-inspiration and end-expiration phases are assumed to have RAC values of 1.5 and 0.5, respectively. The quantitative indicators as a function of RAC are shown in Fig. 9. When RAC is less than 1, the shape indicators are stable to shape errors. With RAC larger than 1, the shape indicators seem to have large changes due to shape errors, which indicates poorly reconstructed images. We suggest $0.7 < \text{RAC} < 1.1$ to achieve good imaging quality from CEIT. Thus, we can conclude that the CEIT can handle small shape errors in referenced CT models. However, the reconstructed images of CEIT will also be distorted if the shape errors are out of the expected range.

E. CT-Derived Starting Models

The starting model may affect the inversion results. We take the CT image as a priori structural information to build

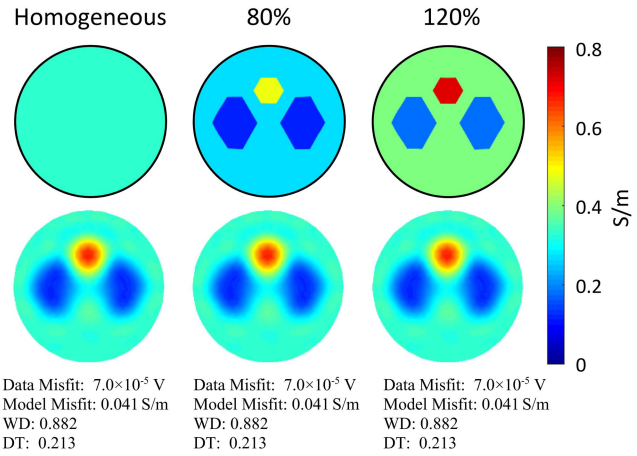

Fig. 10. Results of EIT with homogeneous starting model (left) and starting models that are 80% (middle) and 120% (right) of the true model.

starting models with different conductivity values. Fig. 10 shows the results of conventional EIT with three different starting models. These include a homogeneous model and models with 80%, and 120% of the true conductivity values. The reconstructed images and the quantitative indicators are completely identical, which indicates that conventional EIT cannot produce a better image even if we use a CT-derived starting model with 80% or 120% of the true conductivity model.

IV. Simulations of Thorax Geometry Models

In this section, image reconstructions are performed with increased noise levels in the data to evaluate the robustness of the CEIT against noise. Two cases (Case 1–2) of thoraxes with pathological features are tested (left column of Fig. 11).

A. Modeling

We consider the two models with simulated pathologies depicted in Fig. 11: an injured thorax (Case 1) and a pleural effusion (Case 2). For both scenarios, the conductivities of the heart, lungs and background are set to 0.6 S/m, 0.15 S/m, and 0.33 S/m, respectively, and the corresponding CT values are set to -700 HU, 60 HU, and 30 HU, respectively. The lung injury region and background medium are assumed to have the same conductivities and CT values. The conductivity of the pleural effusion is 0.6 S/m with the same CT value as the background. The recording geometry and the numerical solutions for the forward problems are similar to those in section III. The forward calculations apply a piecewise constant model with a mesh of 2,773 triangular elements and 1,348 nodes. A mesh of 1,385 elements and 737 nodes is used in the inversion problem. A homogeneous conductivity model with $\sigma_0 = 0.33$ S/m is employed for both EIT and CEIT as the starting model.

B. Robustness of CEIT Against Noise

In practical applications, the measured data with noise can be written as

$$\mathbf{v} = \mathbf{v}^* + \boldsymbol{\varepsilon}, \tag{38}$$

where $\mathbf{v}^*$ represents the voltage vector across the boundary of the entire field calculated by CEM, and $\mathbf{v}$ denotes the measured voltage vector with noise ε. In this study, ε is assumed to be a Gaussian noise with mean μ_ε and variance η_ε.

The noise is evaluated by the signal-to-noise ratio (SNR) in this study. For each specific noise level, thousands of independent tests are conducted. Some of the reconstruction results are shown in Fig. 11, and the evolutions of the mean indicators as a function of noise level are plotted in Fig. 12. In particular, we plot the absolute value of the cross-gradient function from the 20 dB tests in Fig. 13 to directly reveal the effectiveness of the constraints from the referenced CT scans.

1) Case 1 (Simulated Injured Lung): We obtain the results of conventional EIT and CEIT using the same regularization factor for each noise level. The regularization parameter α and cross-gradient parameter β are gradually increased for handling with the decreasing SNR. The final data misfit of the two method is close at each noise level. We conclude that in the case of a high SNR, conventional EIT can reconstruct a reasonable image but produces low resolution in the injured area, where CEIT is able to produce a clear image. When the SNR drops to a low value such as 30 dB or 20 dB, conventional EIT can no longer resolve a reliable solution, and the quantitative indicators are increased. However, CEIT can mitigate the distortions from a low SNR due to the use of cross-gradient constraints. The variations in the model misfit, WD, and DT of CEIT are accordingly stable as the SNR decreases. The absolute value of the cross-gradient function during the iterations, shown in the left column of Fig. 13, suggests strong constraints on the edges of the injured lungs and heart.

2) Case 2 (Simulated Pleural Effusion): this test is designed for situations involving incomplete structures in the referenced CT scan. The pleural effusion is designed to be undetected in the CT scan. The parameter selections are similar to those of Case 1. As we concluded for Case 1, the reconstructed images of EIT are distorted due to the low SNR. The areas detected in the referenced CT scan are well reconstructed by CEIT, and the evolution of average quantitative indicators also indicates well reconstructed images of CEIT with respect to the different SNR. Nevertheless, at the low SNRs, the reconstructions of CEIT for the pleural effusion are distorted due to the lack of cross-gradient constraints in this area. The absolute value of the cross-gradient function during the iterations shown in the right column in Fig. 13, which further depicts the outlines of the area with strong cross-gradient constraints.

V. Phantom Experiments

To demonstrate the efficacy of the proposed approach, we utilize the experimental data that were applied in [35]. The experiments consist of four different cases (left column of Fig. 14, Cases 1–4) involving the plastic objects (insulators) with different shapes inserted into a tank.

A. Modeling

In these experiments, the conductivity of the background (saline) is measured as 543 μS/cm. Because CT measurements

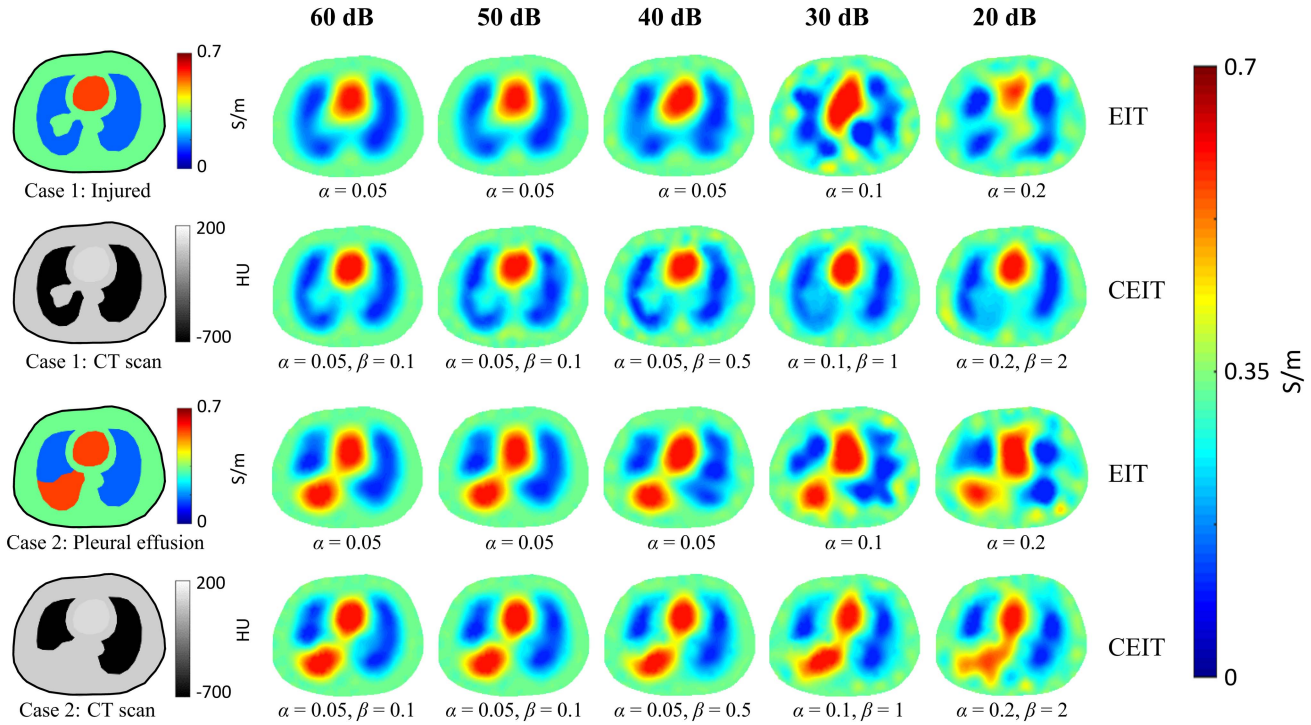

Fig. 11. Reconstructions of injured and pleural effusion examples from noisy numerical tests.

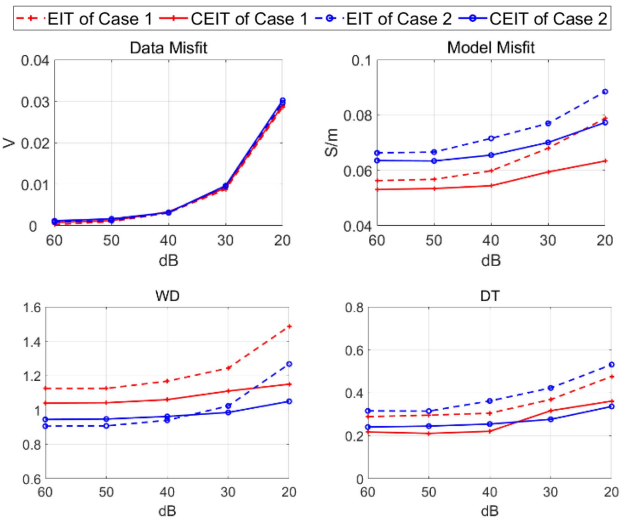

Fig. 12. Evolution of quantitative indicators as a function of noise level.

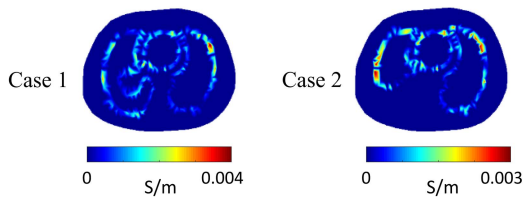

Fig. 13. Absolute value of the cross-gradient function from the 20 dB tests.

are unavailable for the experiments, we simulated approximate CT scan images with 1 HU for saline and 2 HU for the plastic objects in each case, and note that the cross-gradient method mainly utilizes the structure information in the domain of the scan. The contact impedance is measured as $1\times10^{-4}\ \Omega\cdot\mathrm{m}^2$ for all electrodes. The tank data are acquired from the KIT4 recording geometry as described above. The injected current is set to 1 mA with a frequency of 10 kHz. A FEM is applied to numerically approximate a CEM model for forward modeling. The forward and inversion grids applied in this analysis are the same as those used for the simulation of the blocky model in section III. A homogeneous conductivity model with $\sigma_0 = 0.57$ mS/cm is employed as the starting model in all cases.

B. Results and Analysis

The imaging results of Cases 1–4 from EIT and CEIT are shown in Fig. 14. As we can see, EIT reconstructs a reasonable image of the inclusions but with relatively low resolution at the boundaries. The details of the inclusions, especially the sharp edges, are barely distinguished in the images from EIT. Due to the CT image constraints, CEIT reconstructs the targets with improved resolution, recovering the shape of the targets more accurately, and the conductivity contrast is enhanced near the edges of the inclusions. In addition, the reconstructions of the circle inclusion using the two methods in Case 1 are similar. In Cases 2–4, conventional EIT produces a smooth boundary for the inclusions, but CEIT generates sharper reconstructions. Furthermore, in Case 4, when the inclusions are close to one another, the CEIT method is still capable of recovering the inclusions reasonably well. The quantitative indicators are presented in Table III. Both EIT and CEIT yield nearly identical data misfits in each case. In all the testing cases, both EIT and CEIT perform well in reconstructing the major

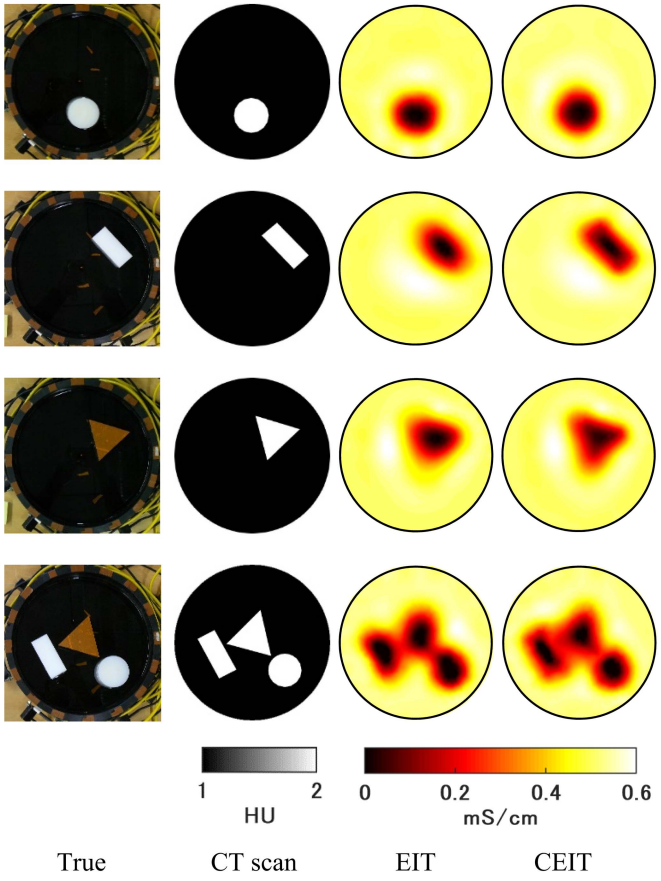

Fig. 14. Reconstructions of phantom experiments with both EIT and CEIT methods. Inclusions are composed of plastic objects. Cases 1–4 are shown from top to bottom.

TABLE III
QUANTITATIVE INDICATORS OF THE RECOVERED INCLUSIONS

	Case1		Case2		Case3		Case4	
	EIT	CEIT	EIT	CEIT	EIT	CEIT	EIT	CEIT
DMS (mV)	0.015	0.015	0.027	0.025	0.022	0.023	0.037	0.038
WD	0.972	0.951	0.933	0.947	0.968	0.942	0.936	0.955
DT	0.190	0.123	0.297	0.178	0.264	0.156	0.308	0.173

shape characteristics, and the WD values are close to the true values in most of the cases. However, the CEIT shows an improvement in DT, which indicates that the CEIT method can better depict the outlines of the inclusions than the conventional EIT.

VI. CONCLUSIONS

The cross-gradient method serves as a link between different medical imaging methods for the same reconstructed target. A CT image-guided electrical impedance tomography method is proposed in this study. CEIT is evaluated by comparing with EIT in both simulations and phantom experiments. The results prove that CT information can be applied to EIT by utilizing the cross-gradient method, thereby providing high resolution images. The simulations of thorax geometry models show that the CEIT method is robust against noise. The further potential of this study is to apply the cross-gradient function to the combinations of different medical imaging methods, resulting in joint approaches that could help improve image quality.

ACKNOWLEDGMENT

The authors would like to thank the inverse problem group at the University of Eastern Finland (UEF), for providing them with the experimental data. They also thank X. Jia, Y. Li, M. A. Meju, L. A. Gallardo, and two anonymous reviewers for helping revise the manuscript.

REFERENCES

[1] L. Martí-Bonmatí, R. Sopena, P. Bartumeus, and P. Sopena, "Multimodality imaging techniques," *Contrast Media Mol. Imag.*, vol. 5, no. 4, pp. 180–189, 2010.
[2] J. Zhang and D. F. Morgan, "Joint seismic and electrical tomography," in *Proc. Symp. Appl. Geophys. Eng. Environ. Problems, Soc. Explor. Geophys.*, 1997, pp. 391–396.
[3] L. A. Gallardo and M. A. Meju, "Characterization of heterogeneous near-surface materials by joint 2D inversion of DC resistivity and seismic data," *Geophys. Res. Lett.*, vol. 30, no. 13, p. 1658, 2003.
[4] L. A. Gallardo and M. A. Meju, "Joint two-dimensional DC resistivity and seismic travel time inversion with cross-gradients constraints," *J. Geophys Res., Solid Earth*, vol. 109, p. B03311, Mar. 2004.
[5] D. Colombo and M. De Stefano, "Geophysical modeling via simultaneous joint inversion of seismic, gravity, and electromagnetic data: Application to prestack depth imaging," *Lead. Edge*, vol. 26, no. 3, pp. 326–331, 2007.
[6] D. J. Brenner and E. J. Hall, "Computed tomography—An increasing source of radiation exposure," *New England J. Med.*, vol. 357, no. 22, pp. 2277–2284, 2007.
[7] S. N. Histed, M. L. Lindenberg, E. Mena, B. Turkbey, P. L. Choyke, and K. A. Kurdziel, "Review of functional/anatomic imaging in oncology," *Nucl. Med. Commun.*, vol. 33, no. 4, p. 349, 2012.
[8] J. G. Webster, *Electrical Impedance Tomography*. New York, NY, USA: Taylor & Francis, 1990.
[9] V. Chitturi and F. Nagi, "Spatial resolution in electrical impedance tomography: A topical review," *J. Electr. Bioimpedance*, vol. 8, no. 1, pp. 66–78, 2017.
[10] T. W. Balmer, S. Vesztergom, P. Broekmann, A. Stahel, and P. Büchler, "Characterization of the electrical conductivity of bone and its correlation to osseous structure," *Sci. Rep.*, vol. 8, no. 1, p. 8601, 2018.
[11] N. Virag, J. M. Vesin, and L. Kappenberger, "A computer model of cardiac electrical activity for the simulation of arrhythmias," *Pacing Clin. Electrophysiol.*, vol. 21, no. 11, pp. 2366–2371, 1998.
[12] N. Chen *et al.*, "Leukemic cell intracellular responses to nanosecond electric fields," *Biochem. Biophys. Res. Commun.*, vol. 317, no. 2, pp. 421–427, 2004.
[13] D. Liu, Y. Zhao, A. K. Khambampati, A. Seppänen, and J. Du, "A parametric level set method for imaging multiphase conductivity using electrical impedance tomography," *IEEE Trans. Comput. Imag.*, vol. 4, no. 4, pp. 552–561, Dec. 2018.
[14] K.-S. Cheng, D. Isaacson, J. C. Newell, and D. G. Gisser, "Electrode models for electric current computed tomography," (in English), *IEEE Trans. Biomed. Eng.*, vol. 36, no. 9, pp. 918–924, Sep. 1989.
[15] T. Murai and Y. Kagawa, "Electrical impedance computed tomography based on a finite element model," *IEEE Trans. Biomed. Eng.*, vol. BME-32, no. 3, pp. 177–184, Mar. 1985.
[16] S. Zlochiver, M. Rosenfeld, and S. Abboud, "Induced-current electrical impedance tomography: A 2-D theoretical simulation," *IEEE Trans. Med. Imag.*, vol. 22, no. 12, pp. 1550–1560, Dec. 2003.
[17] R. P. Patterson and J. Zhang, "Evaluation of an EIT reconstruction algorithm using finite difference human thorax models as phantoms," *Physiol. Meas.*, vol. 24, no. 2, pp. 467–475, 2003.
[18] M. H. Pham and A. J. Peyton, "Computation of 3-D sensitivity coefficients in magnetic induction tomography using boundary integral equations and radial basis functions," *IEEE Trans. Magn.*, vol. 44, no. 10, pp. 2268–2276, Oct. 2008.
[19] N. G. Gencer, M. Kuzuoglu, and Y. Z. Ider, "Electrical impedance tomography using induced currents," *IEEE Trans. Med. Imag.*, vol. 13, no. 2, pp. 338–350, Jun. 1994.

[20] T. J. Yorkey, J. G. Webster, and W. J. Tompkins, "Comparing reconstruction algorithms for electrical impedance tomography," *IEEE Trans. Biomed. Eng.*, vol. BME-34, no. 11, pp. 843–852, Nov. 1987.

[21] M. Cheney, D. Isaacson, J. C. Newell, S. Simske, and J. Goble, "NOSER: An algorithm for solving the inverse conductivity problem," *Int. J. Imag. Syst. Technol.*, vol. 2, no. 2, pp. 65–75, 1990.

[22] J. P. Morucci and P. M. Marsili, "Bioelectrical impedance techniques in medicine, part III: Impedance imaging, second section: Reconstruction algorithms," *Crit. Rev. Biomed. Eng.*, vol. 24, no. 4, pp. 599–654, 1996.

[23] J. P. Morucci, M. Granie, M. Lei, M. Chabert, and P. M. Marsili, "3D reconstruction in electrical impedance imaging using a direct sensitivity matrix approach," *Physiol. Meas.*, vol. 16, no. 3A, pp. A123–A128, 1995.

[24] K. Jerbi, W. R. B. Lionheart, P. J. Vauhkonen, and M. Vauhkonen, "Sensitivity matrix and reconstruction algorithm for EIT assuming axial uniformity," *Physiol. Meas.*, vol. 21, no. 1, pp. 61–66, 2000.

[25] A. Tarantola, "Inversion of seismic reflection data in the acoustic approximation," *Geophysics*, vol. 49, no. 8, pp. 1259–1266, 1984.

[26] P. Chen, T. H. Jordan, and L. Zhao, "Full three-dimensional tomography: A comparison between the scattering-integral and adjoint-wavefield methods," *Geophys. J. Int.*, vol. 170, no. 1, pp. 175–181, 2007.

[27] M. Vauhkonen, D. Vadasz, P. A. Karjalainen, E. Somersalo, and J. P. Kaipio, "Tikhonov regularization and prior information in electrical impedance tomography," *IEEE Trans. Med. Imag.*, vol. 17, no. 2, pp. 285–293, Apr. 1998.

[28] M. Nagao and T. Matsuyama, "Edge preserving smoothing," *Comput. Graph. Image Process.*, vol. 9, no. 4, pp. 394–407, 1979.

[29] K. Zhang, M. Li, F. Yang, S. Xu, and A. Abubakar, "Three-dimensional electrical impedance tomography with multiplicative regularization," *IEEE Trans. Biomed. Eng.*, vol. 66, no. 9, pp. 2470–2480, Sep. 2019.

[30] A. Borsic, B. M. Graham, A. Adler, and W. R. Lionheart. (2007). *Total Variation Regularization in Electrical Impedance Tomography*. [Online]. Available: http://eprints.maths.manchester.ac.uk/

[31] P. Sallee and B. A. Olshausen, "Learning sparse multiscale image representations," in *Proc. Adv. Neural Inf. Process. Syst.*, 2003, pp. 1351–1358.

[32] J. B. Ajo-Franklin, B. J. Minsley, and T. M. Daley, "Applying compactness constraints to differential traveltime tomography," *Geophysics*, vol. 72, no. 4, pp. R67–R75, 2007.

[33] E. T. Chung, T. F. Chan, and X.-C. Tai, "Electrical impedance tomography using level set representation and total variational regularization," *J. Comput. Phys.*, vol. 205, no. 1, pp. 357–372, 2005.

[34] D. Liu, A. K. Khambampati, S. Kim, and K. Y. Kim, "Multi-phase flow monitoring with electrical impedance tomography using level set based method," *Nucl. Eng. Des.*, vol. 289, pp. 108–116, Aug. 2015.

[35] D. Liu, A. K. Khambampati, and J. Du, "A parametric level set method for electrical impedance tomography," *IEEE Trans. Med. Imag.*, vol. 37, no. 2, pp. 451–460, Feb. 2018.

[36] D. Liu, D. Smyl, and J. Du, "A parametric level set-based approach to difference imaging in electrical impedance tomography," *IEEE Trans. Med. Imag.*, vol. 38, no. 1, pp. 145–155, Jan. 2019.

[37] A. Tarantola and B. Valette, "Generalized nonlinear inverse problems solved using the least squares criterion," *Rev. Geophys.*, vol. 20, no. 2, pp. 219–232, 1982.

[38] B. Chen and X. Jia, "Staining algorithm for seismic modeling and migration," *Geophysics*, vol. 79, no. 4, pp. S121–S129, 2014.

[39] D. Zhou, W. Wang, J. Zhang, and D. R. O'Connell, "3D joint inversion of seismic traveltime and gravity data: A case study," in *Proc. SEG Tech. Program Expanded Abstr., Soc. Explor. Geophys.*, 2014, pp. 3148–3152.

[40] J. N. Ogunbo, G. Marquis, J. Zhang, and W. Wang, "Joint inversion of seismic traveltime and frequency-domain airborne electromagnetic data for hydrocarbon exploration," *Geophysics*, vol. 83, no. 2, pp. 9–22, 2018.

[41] J. Zhang, W. Rodi, R. L. Mackie, and W. Shi, "Regularization in 3-D DC resistivity tomography," in *Proc. Symp. Appl. Geophys. Eng. Environ. Problems, Soc. Explor. Geophys.*, 1996, pp. 687–692.

[42] J. Zhang and D. F. Morgan, "Detecting underground caves using joint seismic and electrical imaging method," in *Proc. SEG Tech. Program Expanded Abstr., Soc. Explor. Geophys.*, 1997, pp. 1905–1908.

[43] J. Zhang, "Regularizing data in 3-D DC resistivity tomography," in *Proc. Symp. Appl. Geophys. Eng. Environ. Problems, Soc. Explor. Geophys.*, 1997, pp. 911–915.

[44] R. L. Mackie, F. Miorelli, R. V. Miller, and M. A. Meju, "Seismic image-guided 3D inversion of marine CSEM and MT data," in *Proc. 81st EAGE Conf. Exhib.*, 2019, pp. 1–5.

[45] E. Fregoso and L. A. Gallardo, "Cross-gradients joint 3D inversion with applications to gravity and magnetic data," *Geophysics*, vol. 74, no. 4, pp. L31–L42, 2009.

[46] L. A. Gallardo, "Multiple cross-gradient joint inversion for geospectral imaging," *Geophys. Res. Lett.*, vol. 34, p. L19301, Oct. 2007.

[47] J. Zhou, X. Meng, L. Guo, and S. Zhang, "Three-dimensional cross-gradient joint inversion of gravity and normalized magnetic source strength data in the presence of remanent magnetization," *J. Appl. Geophys.*, vol. 119, pp. 51–60, Aug. 2015.

[48] M. Vauhkonen, J. P. Kaipio, E. Somersalo, and P. A. Karjalainen, "Electrical impedance tomography with basis constraints," *Inverse Problems*, vol. 13, no. 2, p. 523, 1997.

[49] J. Kourunen, T. Savolainen, A. Lehikoinen, M. Vauhkonen, and L. M. Heikkinen, "Suitability of a PXI platform for an electrical impedance tomography system," *Meas. Sci. Technol.*, vol. 20, no. 1, 2009, Art. no. 015503.

[50] C. Gabriel, A. Peyman, and E. H. Grant, "Electrical conductivity of tissue at frequencies below 1 MHz," *Phys. Med. Biol.*, vol. 54, no. 16, p. 4863, 2009.

[51] J. Kaipio and E. Somersalo, "Statistical inverse problems: Discretization, model reduction and inverse crimes," *J. Comput. Appl. Math.*, vol. 198, no. 2, pp. 493–504, 2007.

[52] B. Wördenweber, "Finite element mesh generation," *Comput.-Aided Des.*, vol. 16, no. 5, pp. 285–291, 1984.

[53] C. H. Antink, R. Pikkemaat, J. Malmivuo, and S. Leonhardt, "A shape-based quality evaluation and reconstruction method for electrical impedance tomography," *Physiol. Meas.*, vol. 36, no. 6, p. 1161, 2015.